



**HAL**  
open science

# Porosity estimation in the Fort Worth Basin constrained by 3D seismic attributes integrated in a sequential Bayesian simulation framework

Martin Blouin, Mickaële Le Ravalec, Erwan Gloaguen, Mathilde Adelinet

## ► To cite this version:

Martin Blouin, Mickaële Le Ravalec, Erwan Gloaguen, Mathilde Adelinet. Porosity estimation in the Fort Worth Basin constrained by 3D seismic attributes integrated in a sequential Bayesian simulation framework. *Geophysics*, 2017, 82 (4), pp.M67 - M80. 10.1190/GEO2016-0506.1 . hal-01637241

**HAL Id: hal-01637241**

**<https://ifp.hal.science/hal-01637241>**

Submitted on 17 Nov 2017

**HAL** is a multi-disciplinary open access archive for the deposit and dissemination of scientific research documents, whether they are published or not. The documents may come from teaching and research institutions in France or abroad, or from public or private research centers.

L'archive ouverte pluridisciplinaire **HAL**, est destinée au dépôt et à la diffusion de documents scientifiques de niveau recherche, publiés ou non, émanant des établissements d'enseignement et de recherche français ou étrangers, des laboratoires publics ou privés.

# Porosity estimation in the Fort Worth Basin constrained by 3D seismic attributes integrated in a sequential Bayesian simulation framework

Martin Blouin<sup>1</sup>, Mickaele Le Ravalec<sup>1</sup>, Erwan Gloaguen<sup>2</sup>, and Mathilde Adelinet<sup>1</sup>

## ABSTRACT

The accurate inference of reservoir properties such as porosity and permeability is crucial in reservoir characterization for oil and gas exploration and production as well as for other geologic applications. In most cases, direct measurements of those properties are done in wells that provide high vertical resolution but limited lateral coverage. To fill this gap, geophysical methods can often offer data with dense 3D coverage that can serve as proxy for the variable of interest. All the information available can then be integrated using multivariate geostatistical methods to provide stochastic or deterministic estimate of the reservoir properties. Our objective is to generate multiple scenarios of porosity at different scales, considering four formations of the Fort Worth Basin altogether and then restricting the process to the Marble Falls

limestones. Under the hypothesis that a statistical relation between 3D seismic attributes and porosity can be inferred from well logs, a Bayesian sequential simulation (BSS) framework proved to be an efficient approach to infer reservoir porosity from an acoustic impedance cube. However, previous BSS approaches only took two variables upscaled at the resolution of the seismic data, which is not suitable for thin-bed reservoirs. We have developed three modified BSS algorithms that better adapt the BSS approach for unconventional reservoir petrophysical properties estimation from deterministic prestack seismic inversion. A methodology that includes a stochastic downscaling procedure is built and one that integrates two secondary downscaled constraints to the porosity estimation process. Results suggest that when working at resolution higher than surface seismic, it is better to execute the workflow for each geologic formation separately.

## INTRODUCTION

In the oil and gas industry, the inference of petrophysical properties such as porosity and permeability is a key step in the construction of reservoir grids used for numerical modeling of dynamic processes (Le Ravalec et al., 2014). For such applications, those properties are often derived from well logs and are measured at a high vertical sampling rate. However, in petroleum reservoir characterization, due to the expensive nature of drilling at high depth, the availability of those measurements remains restricted. Thus, the sparse set of direct measurements of the target variables prevents the use of classical univariate geostatistical and interpolation methods to provide accurate 3D models of the reservoir properties usable by the reservoir engineer (Goovaerts, 2000). Because 3D seismic data are routinely acquired in hydrocarbon reservoir characterization, rock-physics approaches can be used to invert for properties of interest directly from seismic data with statistical (Grana, 2014; Fang and Yang, 2015) or determin-

istic methods (Adelinet and Le Ravalec, 2015). Advantages of such an inversion scheme include better calibration to seismic traces and log data as well as simultaneous estimation of multiple reservoir parameters and more accurate property prediction further from the well (Grana and Della Rosa, 2010). On the flip side, generating estimation for more than one variable in a single step supposes that corresponding data have the same level of noise and resolution. It also puts a high level of confidence on the 3D seismic data and assumes stationarity of the petrophysical relationship (Sauvageau et al., 2014).

Another way to consider the problem is to first proceed with the inversion (Tarantola, 1984) of the seismic data (prestack or poststack/stochastic or deterministic) and use the resulting model to constrain the simulation of reservoir properties with geostatistical tools (Dubrule, 2003). The petroleum industry has seen the uprise of numerous multivariate geostatistical methods to produce 2D or 3D grid estimates of various physical properties at different scales (Haas and Dubrule, 1994; Pyrcz and Deutsch, 2014). Those rock-property es-

Manuscript received by the Editor 28 September 2016; revised manuscript received 22 February 2017.

<sup>1</sup>IFP Energies Nouvelles, Rueil-Malmaison Cedex, France. E-mail: martin.blouin@ete.inrs.ca; mickaele.le-ravalec@ifpen.fr; mathilde.adelinet@ifpen.fr.

<sup>2</sup>INRS-ETE, Québec, Canada. E-mail: erwan.gloaguen@ete.inrs.ca.

© 2017 Society of Exploration Geophysicists. All rights reserved.

timates can integrate disparate data sources and can be achieved at locations where ground truth measurements are unavailable (e.g., Doyen, 1988).

To use secondary data (seismic) in a flexible way, permitting non-linear and non-Gaussian relationships to hard data, Doyen et al. (1997) propose the use of a sequential algorithm in a Bayesian framework that is called Bayesian sequential simulation (BSS). The main feature of this algorithm is the use of a joint relationship that links the estimated parameter to an external, more densely sampled attribute (3D seismic). It was then applied by Dubreuil-Boisclair et al. (2011) to estimate hydraulic conductivity from radar tomog-

raphy data. The approach was extended later on to multimodal joint relationships for gas-hydrate volume estimation (Dubreuil-Boisclair et al., 2012). It was also applied in a two-step simulation process for a hydrogeologic application with a downscaling procedure (Ruggeri et al., 2013). All applications helped to integrate successfully geophysical data from different methods at various scales to generate 2D and 3D maps of the properties of interest measured at boreholes.

In this paper, the BSS algorithm is used to generate multiple realizations of porosity  $\phi$  using 3D prestack deterministic seismic inversion results as secondary data. The data integration methodology is applied to the Fort Worth Basin geologic formations in northern Texas. First, multiple 3D porosity fields are generated for all four principal geologic formations at the scale of the seismic data. Second, a Bayesian downscaling procedure integrated to the workflow is then used to generate in single-step multiple porosity scenarios at a scale more suited to geologic modeling. Third, the effect of adding supplemental constraints in the joint relationship from the inversion results is studied. The high-resolution results with and without further constraints are compared for only one geologic formation, the Marble Falls (MF) limestones, making it possible to observe intra-formation details at a smaller scale.

## DATA AND GEOLOGIC CONTEXT

The studied reservoir is located in the Fort Worth Basin of northern Texas (Figure 1a), a region that is home to a well-known unconventional natural-gas reservoir (Montgomery et al., 2005). The region includes the very productive Barnett Shale that has been exploited by several companies for many years (Bowker, 2007). The interest in the integration of seismic attributes with geologic and well-log data has been recognized in this region to produce facies models (Marroquín, 2015) and physical property estimation (Naeem et al., 2015) to improve field development and production.

The basin was formed during the Paleozoic era, mainly Mississippian and Pennsylvanian. Its presence is related to the formation of the Muenster arch to the northeast and the Ouachita front to the southeast (Figure 1a). The basin is bounded to the west by the pre-Mississippian Bend Arch, which is an extension of the Llano uplift toward the north. A specific portion of the stratigraphic sequence of the basin (Pollastro et al., 2007) is investigated. It includes four geologic formations ranging from oldest to youngest: the Ellenburger Limestone, the Barnett Shale, the MF limestone, and the clastic Bend Formation (Figure 1b). The transition between the Bend Formation and MF is characterized by sharp variations in physical properties, such as the acoustic impedance  $I_P$ , shear impedance  $I_S$ , and porosity  $\phi$ . The Barnett Shale has comparable  $I_P$  values with the Bend, but shows different  $I_S$ . Erlich and Coleman (2005) observe that MF is characterized by lateral variations in thickness and present differences in geologic facies between the upper and the lower parts. Log measurements in Figure 1b exhibit the distinct characters of the geologic units between its upper and lower sections. This high nonstationarity in geology and its petro-physical properties prevent the use of conventional geostatistical tools.

The inverted seismic data used in this study are coming from a 3D survey covering 230 km<sup>2</sup> that was collected in 2005 and 2006 in Hamilton County, Texas. For the purpose of this study, the test area is limited to a 2 km<sup>2</sup>, corresponding to 41 inline and 41 crossline bins with a size of 33.5 × 33.5 m each. The cropped volume was chosen such that well 1 lies approximately at the center of the seismic cube. Prestack deterministic seismic inversion was computed

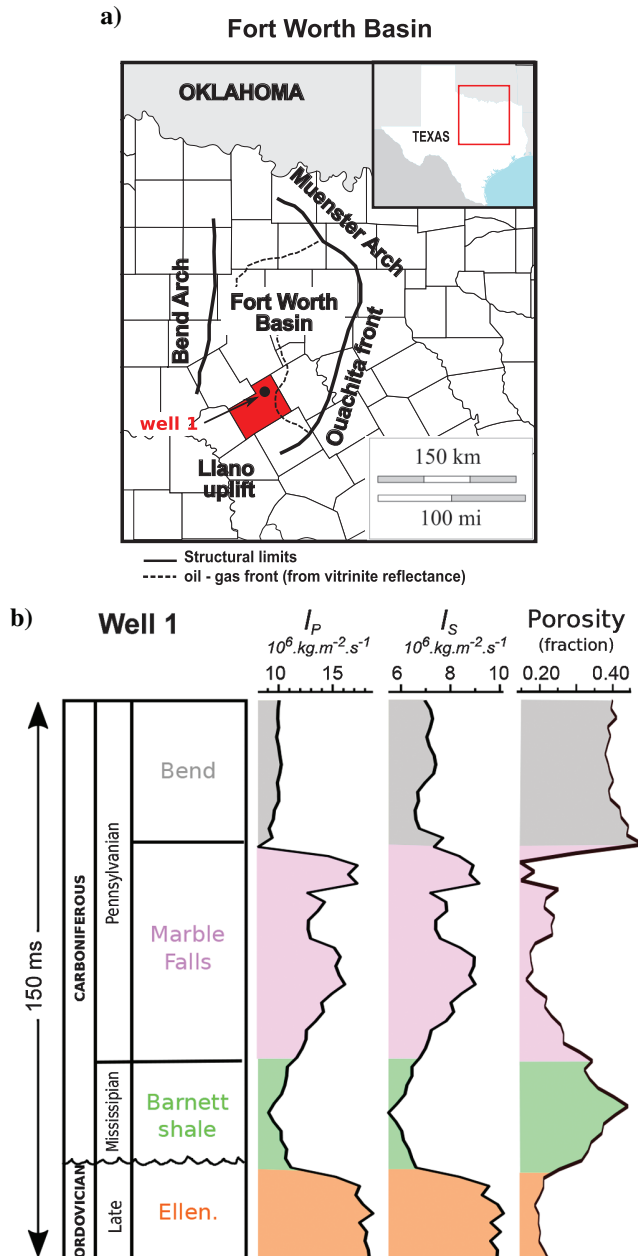


Figure 1. (a) Location of the Fort Worth Basin with the studied area in red and (b) formations, porosity, P- and S-wave impedances measured along well 1 upscaled at seismic resolution (2 ms). Modified from Adelinet and Le Ravalec (2015).

on the data sets providing  $I_P$ ,  $I_S$ , and density cubes over the whole domain (the four investigated formations). The inversion methodology is presented in Adelinet et al. (2013) as well as a work extension to azimuthal inversion. Orthogonal panels of the outputs from the inversion procedure are presented in Figure 2a–2c. Figure 2d displays the relative geologic age associated with each cell. The latter information is rather an input than an output to the seismic inversion procedure, and it is calculated from major seismic horizons and the associated formation deposition mode. This information permits the inversion procedure to be geologically consistent and will serve as such for the geostatistical simulation process presented in this paper.

## METHODOLOGY

Our objective is to estimate porosity in the Fort Worth Basin. To achieve our goal, we adapt an existing algorithm to the geologic setup of the region and to available data that are common for unconventional reservoir characterization.

### Hypothesis

In this study, we aim to simulate porosity realizations given the well-log porosity  $\phi$  and an acoustic impedance  $I_P$  model. The porosity  $\phi$  is known at a few points only; it is the primary variable. Also,  $I_P$  is known over the whole grid; it is the secondary variable. We hypothesize that the statistical relationship between these variables can be inferred from well logs in the form of a likelihood, and that this likelihood can be used to constrain the stochastic realizations of porosity. It also requires that a prior distribution of the primary variable ( $\phi$ ) can be estimated through its geologic prior, covariance, and well-log hard data. With the prior and likelihood elements, the Bayes theorem states that one can calculate the posterior distribution of a random variable of interest by multiplying them:

$$P(\phi|I_P) = \frac{P(I_P|\phi)P(\phi)}{P(I_P)}, \quad (1)$$

with  $P(A)$  being the probability of  $A$  and  $P(A|B)$  being the probability of  $A$  knowing  $B$ .

### The Bayesian sequential simulation

The BSS algorithm is a stochastic and sequential geostatistical simulation procedure aiming at solving equation 1 sequentially over space. It uses a sequential simulation scheme, visiting cells of a domain randomly and picking from a distribution in the same fashion (Hammersley, 2013). For each realization, the estimation of the primary variable at each cell (2D) or pixel (3D) is achieved one by one, sequentially. The posterior variable distribution from which the value is randomly picked is determined as the product of a prior ( $P(\phi)$  in equation 1) distribution by a selected likelihood function ( $P(I_P|\phi)$  in equation 1), based on an extensively sampled secondary attribute (see the workflow in Figure 3).

#### Step 1 — Prior distribution $P(\phi)$

If the variable under study is unimodal and shows a Gaussian distribution, the estimation of the prior distribution at any grid nodes consists of inferring the conditional mean and variance of the Gaussian distribution at a grid-node location knowing previously simulated nodes and measured data. As shown by Matheron et al. (1987), the conditional mean and variance of a multi-Gaussian regionalized variable (the variable that shows a spatial structure) can be assessed through the use of simple kriging in space (Figure 3a).

In the case in which the primary variable distribution is multimodal, a set of conditional means and variances for each mode (family) must be defined. For the case of a distribution presenting a multi-Gaussian shape, it can be approximated and modeled by a Gaussian mixture model (GMM). From the secondary attribute ( $I_P$  in our case)

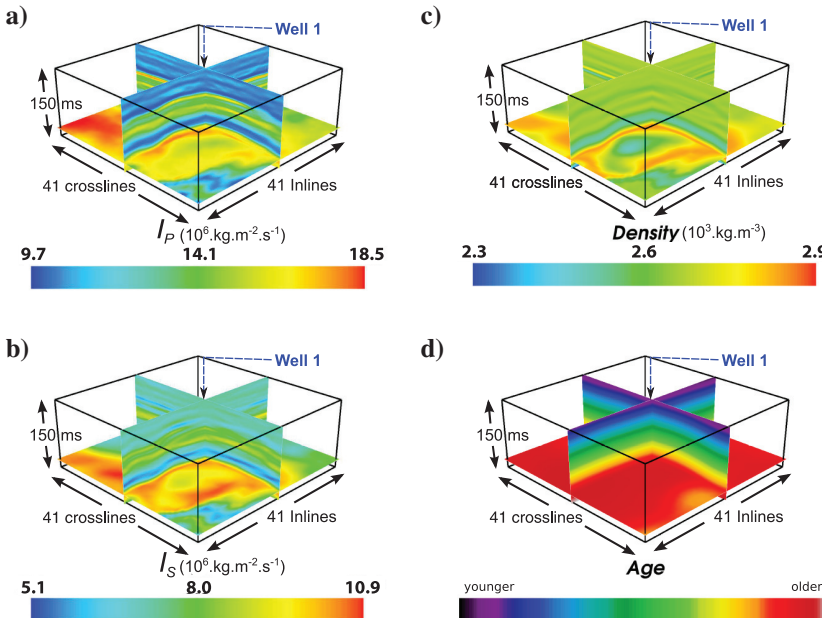


Figure 2. The 3D seismic attributes resulting from the deterministic stratigraphic inversion (Adelinet et al., 2013) operated on prestack seismic data over the study subregion. (a) The P-impedance output in  $10^6 \text{ kg m}^{-2} \text{ s}^{-1}$ , (b) S-impedance output in  $10^6 \text{ kg m}^{-2} \text{ s}^{-1}$ , (c) density output in  $10^3 \text{ kg m}^{-3}$ , and (d) relative geologic age input.

of the randomly selected grid cell, the probability to be in a given family can be calculated from the joint distribution. The family is randomly picked by providing the mean, variance, and variogram model for simple kriging. Considering two families FAM1 and FAM2, the probability  $P$  of a cell  $i$  of belonging to FAM1:

$$P(\text{FAM1}) = \frac{\int f(\phi^{\text{FAM1}}|I_P^{\text{FAM1}})}{\int f(\phi|I_P)}, \quad (2)$$

where  $f(\phi|I_P)$  is the likelihood function extracted from the bivariate PDF for a known  $I_P$  at cell  $i$  and  $f(\phi^{\text{FAM1}}|I_P^{\text{FAM1}})$  is the same likelihood function but calculated using samples from family one only.

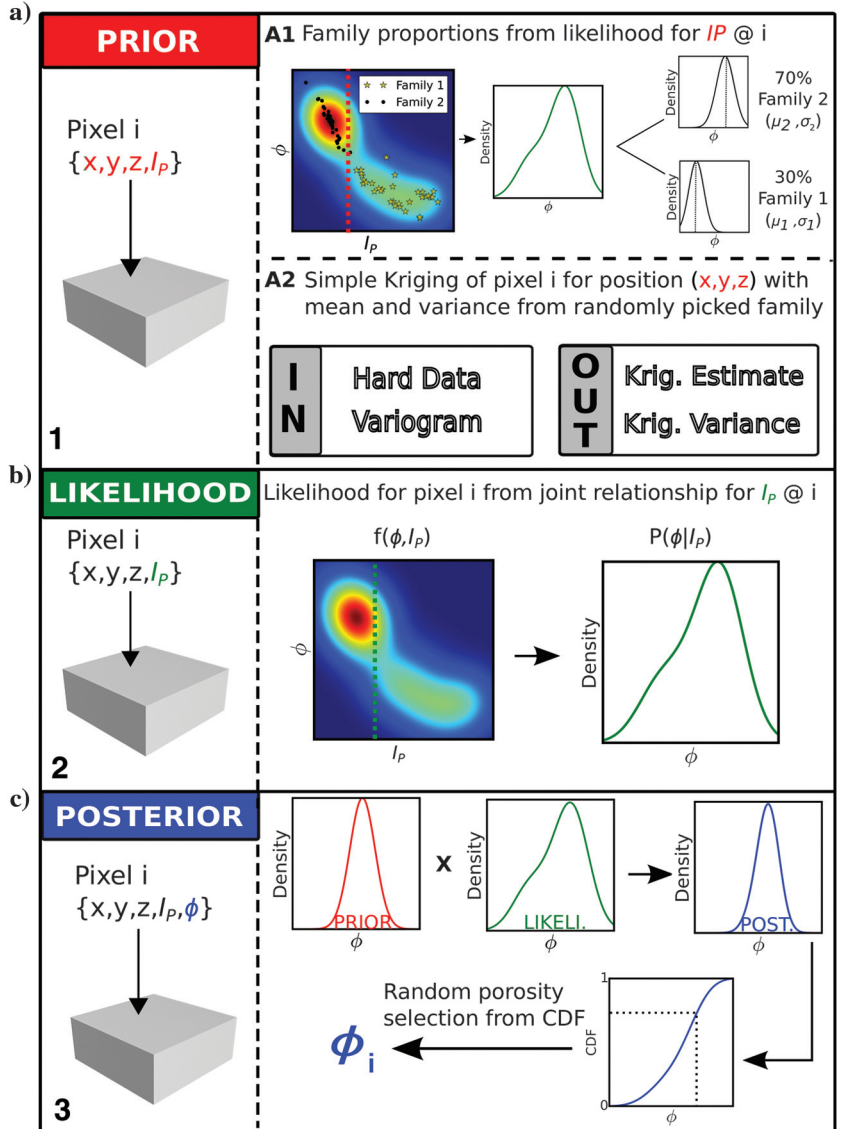
Similar to the unimodal case, according to the available hard data and the previously simulated cells, simple kriging is used to compute the conditional means and variances: They provide the necessary parameters to build the prior conditional probability density function (PDF).

### Step 2 — Kernel density estimation

A major contribution of Doyen (1988) was to propose an efficient way to transform the discrete crossplot of the primary and secondary variables measured at wells into a continuous statistical joint relationship  $P(I_P|\phi)$  in equation 1. However, it is worth mentioning that  $P(I_P|\phi)$  is inferred using seismic data derived from sonic logging at the well, but for the inference outside the wells, surface seismic data are used. This huge difference in log surface seismic resolution will be further discussed in a subsequent section. With no prior assumption made about the joint behavior of  $I_P$  and  $\phi$ , the bivariate PDF that defines this relation is estimated using a nonparametric kernel density estimator (KDE) (Rosenblatt, 1956; Parzen, 1962). Using the KDE formulation by Wand and Jones (1995), a continuous bivariate function is defined as (Figure 3b)

$$f(\phi, I_P) = \frac{1}{nh_1h_2} \sum_{i=1}^n K\left(\frac{\phi - \phi_i}{h_1}\right) K\left(\frac{I_P - I_{Pi}}{h_2}\right), \quad (3)$$

Figure 3. Schematic description of the BSS workflow. Prior construction from hard data (1), likelihood determination from secondary attribute (2), and posterior of the primary variable (3).



where  $h_1$  and  $h_2$  are the estimator respective bandwidths for each variable,  $n$  is the number of samples, and  $K$  is the kernel function. Both bandwidth estimations are data driven, and they are first estimated using empirical methods (Silverman, 1986). However, the final bandwidth values used for the KDE are manually adjusted from those estimations to prevent border effects and cover all possible values represented in the  $I_P$  cube and other secondary attributes. In addition, bandwidth has to be large enough to avoid discontinuities on the marginal likelihood function, but if it is too large, the smoothing effect on the result will be considerable. Hence, a user intervention is required for this selection. As the kernel estimation is done on multi-Gaussian continuous variables, we used a  $K$  Gaussian kernel

$$K(x) = \frac{e^{-\frac{x^2}{2\pi}}}{\sqrt{2\pi}}. \quad (4)$$

After the preprocessing procedure, the likelihood function estimation is straightforward (Figure 3b). As in the first step of the prior definition, a slice of the bivariate PDF is extracted according to the secondary attribute value at the selected cell location.

### Step 3 — Posterior distribution

After normalization of the prior and likelihood, the posterior (equation 1) is calculated by multiplying of the two (Figure 3c). The resulting PDF can now be converted to a cumulative density function, and a value is randomly picked and assigned to the selected grid node. This new value is now considered as a data point that is included in the kriging system for subsequent prior distribution computation (Figure 3c).

Steps 1–3 are repeated until all the nodes of the grids are visited once.

## Bayesian downscaling procedure

In our case and more often for reservoir characterization purposes, the seismic data (secondary variable) are on a grid tens of times coarser on the vertical axis than the well log (primary variable). Up to this point, the methodology presented either assumes that the primary and secondary are sampled at the same resolution or neglects the size difference between the two supports. One way to convert all the data at the same scale consists of upscaling logs of  $\phi$  and  $I_P$  to the seismic grid resolution at the beginning of the workflow. If upscaling is chosen, all workflow steps discussed above can be applied as it is.

Another way to handle the scale or resolution issues is to choose a downscaling approach. Indeed, seismic resolution is often not precise enough to provide an adequate level of heterogeneity characterization for reservoir engineering purposes (the surface seismic wavelength averages a large vertical volume missing critical heterogeneous geologic features driving hydrocarbon recuperation). Provided that there are available higher resolution measurements compared with the seismic signal (at the well), assuming that the surface seismic signal at depth is consistent with these in situ data and verifying that both are correlated, a joint downscaling kernel can be constructed as

$$f(I_P^{\text{HR}}, I_P^{\text{LR}}) = \frac{1}{nh_1h_2} \sum_{i=1}^n K\left(\frac{I_P^{\text{HR}} - I_{Pi}^{\text{HR}}}{h_1}\right) K\left(\frac{I_P^{\text{LR}} - I_{Pi}^{\text{LR}}}{h_2}\right), \quad (5)$$

with  $I_P^{\text{HR}}$  and  $I_P^{\text{LR}}$ , the acoustic impedance measured at high resolution (well log) and low resolution (seismic data), respectively. The resulting bivariate PDF provides the basis for switching from low resolution  $I_P$  (inverted cube) to high resolution  $I_P$  (well) in a Bayesian framework. To simulate high-resolution porosity, the high-resolution joint relationship between the primary and secondary variable is also necessary:

$$f(\phi^{\text{HR}}, I_P^{\text{HR}}) = \frac{1}{nh_1h_2} \sum_{i=1}^n K\left(\frac{\phi^{\text{HR}} - \phi_i^{\text{HR}}}{h_1}\right) K\left(\frac{I_P^{\text{HR}} - I_{Pi}^{\text{HR}}}{h_2}\right). \quad (6)$$

Both relationships are integrated to the likelihood estimation workflow (Figure 3b), replacing the single bivariate PDF used for low-resolution simulations by a multivariate kernel. The likelihood that will relate high-resolution porosity values to seismic scale  $I_P$  at a given location in the cube (for a given seismic scale  $I_P$  value) is the result of the scalar product of the corresponding downscaling likelihood with the integral high-resolution joint PDF:

$$P(\phi^{\text{HR}} | I_P^{\text{LR}}) \propto f(I_P^{\text{HR}} | I_P^{\text{LR}}) \times \int f(\phi^{\text{HR}}, I_P^{\text{HR}}). \quad (7)$$

## BSS with three constraints

Conventional prestack stratigraphic inversion permits us to compute three physical variables ( $I_P$ ,  $I_S$ , and density) presenting strong statistical and physical relations with porosity, the rock matrix, its porosity, and the filling fluids (Gassmann, 1951; Batzle and Wang, 1992). Because additional information on porosity fluctuations in the cube of interest is contained in  $I_S$  and density cubes, we investigate the possibility of adding a second set of secondary data in the BSS framework. Once again, only the likelihood estimation needs to be modified in the workflow in Figure 3b. In that case, the KDE estimator for the 3D case is given by

$$f(\phi, I_P, I_P') = \frac{1}{nh_1h_2h_3} \sum_{i=1}^n K\left(\frac{\phi - \phi_i}{h_1}\right) \times K\left(\frac{I_P - I_{Pi}}{h_2}\right) K\left(\frac{I_S' - I_{Si}'}{h_3}\right), \quad (8)$$

with  $I_S'$  corresponds to  $I_S$  normalized by  $I_P$ . This normalization enhances the relation with the primary variable  $\phi$ :

$$I_S' = \frac{I_S}{I_P}. \quad (9)$$

## Results

This section presents the resulting scenarios of porosity estimate in the described region of the Fort Worth Basin. Three cases are treated, following the three implementations described in “Methodology” section.

## Upscaled BSS

For the first case, porosity scenarios were simulated on a grid with the vertical resolution equivalent to the vertical seismic sampling, which is 2 ms in this study. The lateral cell extension was also in agreement with seismic data binning, and was of 33.5 m in each direction. We refer hereafter to lateral variations as increments of inline and crossline seismic bins. The data under consideration are the seismic  $I_P$  and the upscaled logs for  $I_P$  and  $\phi$ . Well-log data are gridded to seismic time steps using a simple linear interpolation of the original high-resolution irregularly sampled measurements. The four formations are treated as a single one.

### Preprocessing

The preprocessing steps are hard data histogram modeling using GMM, computation, and modeling of the variogram of the porosity and construction of the kernel between  $I_P$  and  $\phi$ . From Figure 4a, a

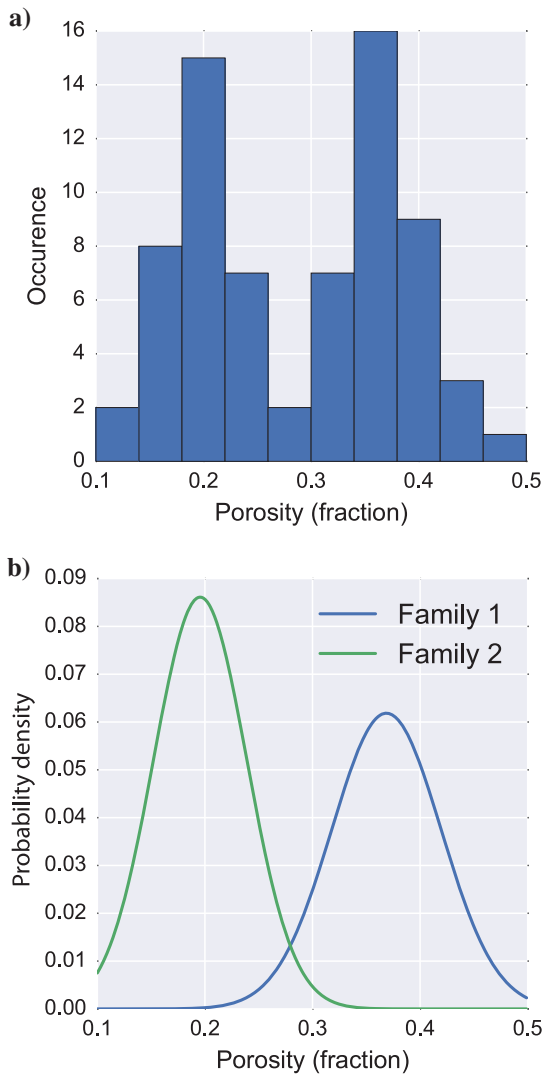


Figure 4. (a) Histogram of porosity data at well 1 upscaled at seismic resolution (2 ms) and (b) modeled PDF of each family from bimodal GMM approximation.

fair assumption can be made that the upscaled porosity-log distribution over the four investigated formations is bimodal. Hence, the GMM procedure is constrained to two Gaussians with distinct means and variances, as presented in Figure 4b. Statistics from each family are used for the simple kriging procedure as described in the workflow.

The vertical variogram is modeled on the experimental variogram computed using upscaled porosity logs as a function of the relative sediment deposition time logs on well 1. For the horizontal range, because only one well is available, an assumption is made that the horizontal range of the variogram of the porosity can be approximated by the horizontal range of the seismic  $I_P$  cube. However, because  $I_P$  has been computed using least-squares algorithms, the horizontal range is certainly overestimated. But, with only one well, this is the best approximation that can be made at this stage and using these data. The experimental variogram is calculated on the deposition time consistent  $I_P$  cube to ensure consistency with prior geologic model. Ranges, model types, and relative nugget values are presented in Table 1.

To generate the joint  $(\phi, I_P)$  kernel, the collocated upscaled well-log measurements over the investigated vertical interval are used. Boundaries of the relationship (minimum and maximum value for each variable) are chosen to ensure complete coverage of the range of  $I_P$  values contained in the inverted cube and to honor the sampled porosity at well 1. Figure 5 displays the 75 data points used to con-

Table 1. Variogram parameters used for simple kriging.

	Vertical <sup>3</sup>	Horizontal <sup>4</sup>
Nugget	5%	5%
Model	Spherical	Spherical
Range	10 ms	20 bins ( $\approx 660$ m)

<sup>3</sup>The vertical variogram is calculated along well 1 (the range is in milliseconds).  
<sup>4</sup>The horizontal variogram is calculated on seismic data along isochrones slice (the range is in number of seismic bins).

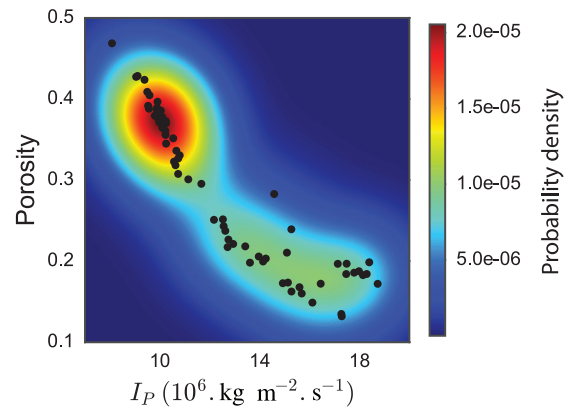


Figure 5. Bivariate PDF generated by 75 collocated upscaled well-log measurements (black dots) of the acoustic impedance ( $10^6 \text{ kg m}^{-2} \text{ s}^{-1}$ ) and porosity. The red color represents a high density of probability, whereas blue refers to a low density of probability.

struct the relationship along with the intensity of the bivariate PDF built from equation 3.

The PDF clearly exhibits two families (family 1 showing  $\phi$  interval [0.25–0.45] and  $I_p$   $[8 - 10] \times 10^6 \text{ kg m}^{-2} \text{ s}^{-1}$  and family 2 showing  $\phi$  interval [0.1–0.25] and  $I_p$   $[12 - 20] \times 10^6 \text{ kg m}^{-2} \text{ s}^{-1}$ ), which overlap for certain  $I_p$  values (in  $10^6 \text{ kg m}^{-2} \text{ s}^{-1}$ ). Scattering is more important in the low-porosity section of the data.

### Porosity realizations

One hundred simulated low-resolution porosity cubes have been generated using the BSS algorithm presented in Figure 3, i.e., at the vertical seismic scale of regular 2 ms intervals. The 3D grid consisted of 126,075 elements equally spaced, and 75 well-log measurements of porosity have been used as hard data. Figure 6a and 6b displays two orthogonal vertical panels that cross in the middle of the cube (close to well 1) and a time slice located mainly in the MF formation of a randomly chosen realization.

From the two vertical panels (Figure 6a and 6b), we see the clear distinction between the four investigated formations. The large-scale trends are well-respected, and some heterogeneity is generated within the formations. However, these features are not clearly present in the

low-porosity end and the distinction between the top and bottom MF is not evident at this scale. Figure 6d presents a histogram that is bimodal, like the hard-data distribution, but that increases the occurrence of mean values. This is the consequence of our algorithm that does not reproduce the hard-data histogram, but that generates a compromise with a secondary attribute following the joint relationship.

Figure 7 presents the mean and standard deviation pixel by pixel of the 100 realizations. The mean panel (Figure 7a and 7c) features are consistent with what is shown on the realization in Figure 6, telling us that all realizations follow the large-scale trends and some intraformation features. Distinctions between the top and bottom MF can be observed, meaning that it is reproduced to some degree by the algorithm. Figure 7b and 7d shows the lateral effects of the hard data and the small amount of uncertainty introduced in the simulation process. Indeed, among others, we neglected the uncertainty coming from the change of scale and constrained our results with an attribute from a deterministic inversion, which is considered exact.

### Downscaled BSS

In this section, we applied the downscaling approach in a Bayesian framework as described in equation 7. For practical purposes (com-

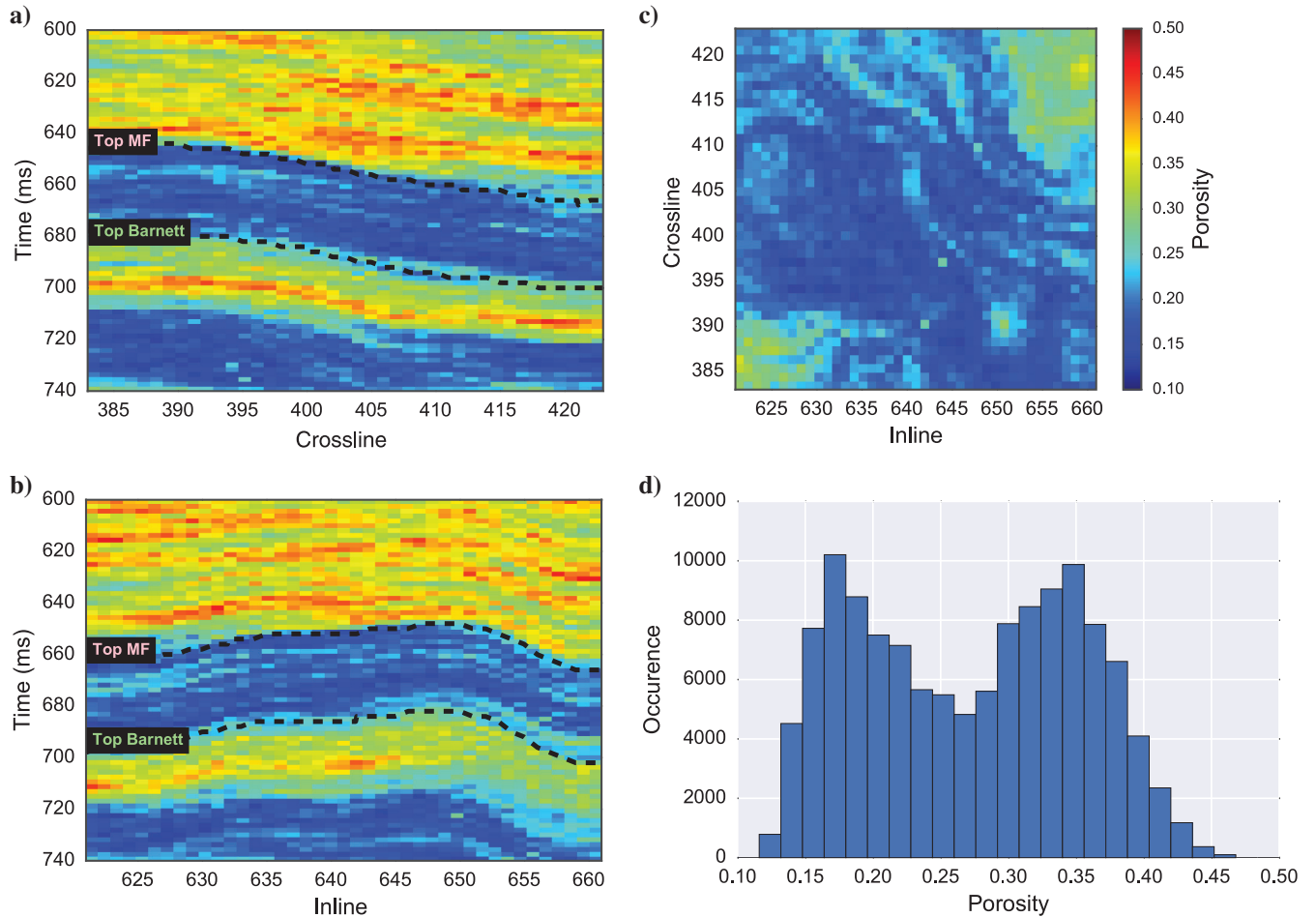


Figure 6. BSS porosity simulation result example at the seismic scale. (a) Vertical panel at inline = 641, (b) vertical panel at crossline = 403, (c) horizontal panel at time = 670 ms, and (d) histogram of the displayed realization.



putting time, memory usage, useless for dynamic simulations, etc.), we upsampled the log data by four with a vertical spacing of 0.5 ms.

#### Downscaling procedure

In equation 2, we build the joint  $I_p$  downscaling kernel with well-log measurements at the desired simulation scale (0.5 ms) collocated with low-resolution seismic inversion results. To match the frequency of the high-resolution measurements, we used the nearest neighboring seismic cell. Figure 8 displays the bivariate function produced by a KDE along with corresponding data points.

The scatter plot (Figure 8) clearly shows the range difference between the  $I_p$  log data and the inverted  $I_p$ . This behavior was expected because the tool used to measure sonic in a well and determine  $I_p$  operates at frequencies way higher (10–40 kHz) than surface seismic (10–50 Hz). Hence, we expect higher variability from the well-log measurements because they detect finer impedance changes. There is also a phenomenon called frequency-dependent velocity or dispersion (e.g., Batzle et al., 2006; Adelinet et al., 2011) that causes a discrepancy between low- and high-resolution

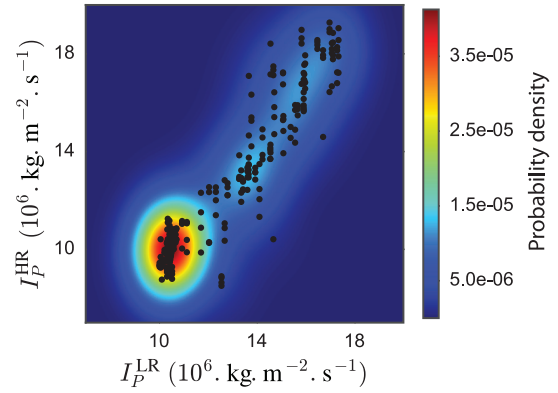


Figure 8. Bivariate downscaling PDF generated by 300 acoustic impedance well-log measurements collocated with seismic data (black dots). The red color represents a high density of probability, whereas blue refers to a low density of probability. The  $I_p^{LR}$  representing the acoustic impedance at seismic resolution (2 ms) and  $I_p^{HR}$ , the higher resolution IP from the well log (500  $\mu$ s). The  $I_p$  unit is in  $10^6 \text{ kg m}^{-2} \text{ s}^{-1}$ .

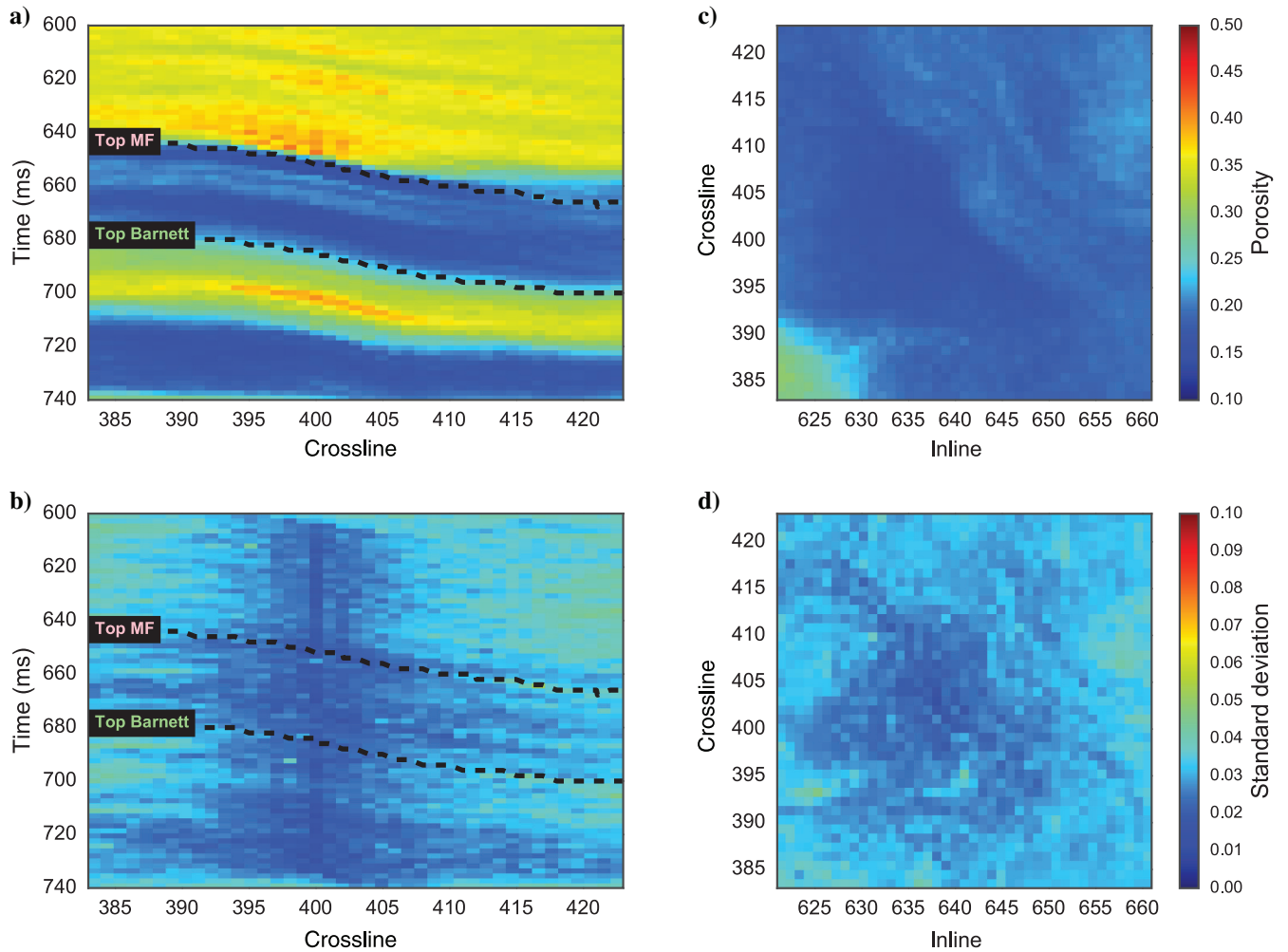


Figure 7. Mean and standard deviation pixel by pixel of the 100 low-resolution simulations. (a) Mean vertical panel at inline = 641 with (b) its associated standard deviation, (c) mean horizontal slice at time = 670 ms, and (d) its associated standard deviation.

measurements. We expect that the introduction of this downscaling joint relationship in our methodology statistically compensates for that effect. Following equation 6, for every cell visited by the algorithm, the likelihood is taken as a slice of the downscaling kernel multiplied by the integral of the joint relationship  $f(I_p|\phi)$ . By construction, this is going to introduce a larger uncertainty in our result.

### High-resolution porosity realizations

Using the BSS algorithm with the integrated downscaling procedure, 100 realizations were computed. The simulated porosity cubes have 499,257 cells, corresponding to a vertical spacing (0.5 ms) four times smaller than the seismic scale. At this scale, 300 well-log measurements from well 1 are used as hard data. A realization example is presented in Figure 9.

From the two vertical panels (Figure 9a and 9b), we see finer layering compared with the low-resolution case. Some intraformation features are present, and the general geologic structure is respected. However, the distinction between the four formations is not so clear anymore, showing smooth rather than sharp transitions. Moreover, we guess from the three panels and observe clearly on the histogram (Figure 9d) that the occurrence of mean values has increased dramatically and that it is harder to distinguish two families

(one high porosity/one low porosity). While considering the integral of the joint relationship  $f(\phi, I_p)$ , the downscaling procedure integrates the statistics of both families everywhere in the simulation domain.

The same diagnostic comes from looking at the mean and standard deviation of the 100 realizations (Figure 10). The transition between formations is not as sharp as the geology would suggest. Porosity values within formations of both families are pushed toward the global mean getting them closer one to another. Still, the figure shows that we successfully added some desired uncertainty from the scale change and the misfit between the inverted and well-log data.

Downscaling is mathematically always advantageous if one is able to build a reliable kernel between low seismic impedance and high-resolution log impedance. However, as in the case of the entire Fort Worth Basin (all four investigated formations) porosity estimation, the authors agree that the results of the downscaling procedure are debatable, mainly because of the lack of accuracy of the KDE for low acoustic impedances.

### On adding more constraints

In this subsection, we test the effect of adding another secondary attribute has a constraint to build the likelihood (equation 8). We test

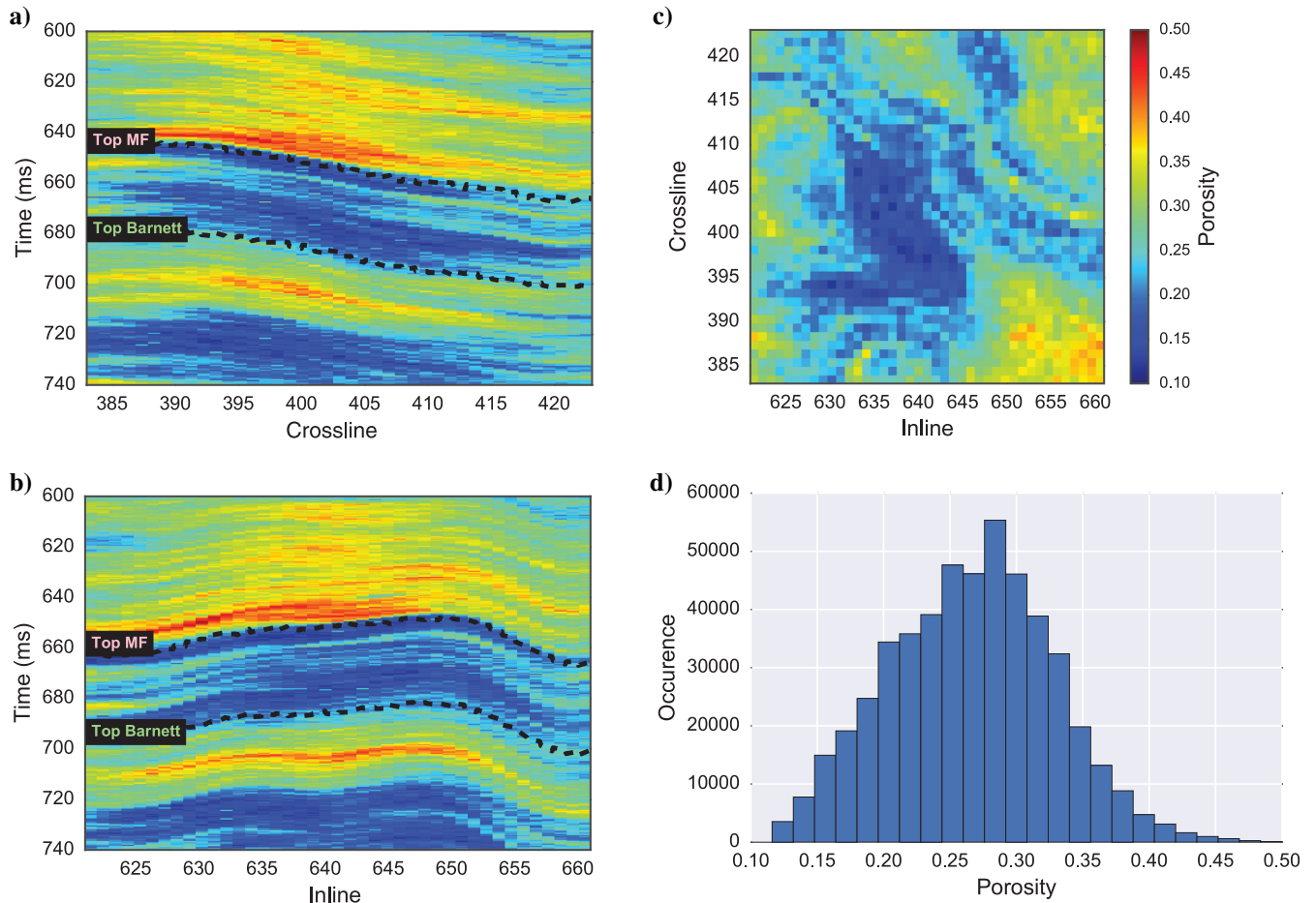


Figure 9. Downscaled BSS porosity simulation result example. (a) Vertical panel at inline = 641, (b) vertical panel at crossline = 403, (c) horizontal panel at time = 670 ms, and (d) histogram of the displayed realization.

the approach at higher resolution than the seismic scale (the same vertical spacing as in the previous section), and we work in a sub-domain corresponding to the MF only (see Figure 2b). We limit the domain of simulation to prevent incorporating high porosity values in this nonporous formation as a consequence of the downscaling procedure.

#### Preprocessing for MF

As we did before for the four formations altogether, we modeled the hard-data histogram with GMM, we constructed joint relationships and modeled the variogram for the MF formation. The variogram parameters used are the same as the ones presented in Table 1. In the MF, a bimodal distribution is also represented in the porosity histogram (Figure 11a) and it can be modeled with two Gaussian functions (Figure 11b). This is consistent with the geologic interpretation that distinguishes two MF subformations (top and bottom).

To use the BSS algorithm scheme in the MF with one secondary attribute as a constraint, collocated well-log measurements of the hard and secondary attribute at a resolution of 0.5 ms are used to generate the joint PDF at a following equation 3. The resulting bi-

variate relationship along with the 67 data points are presented in Figure 12.

To further constrain our realizations with another secondary attribute, the dimension of the relationship in Figure 12 has to increase by one. Hence, by using equation 7 along with the collocated data  $I_P$ ,  $I'_S$ , and  $\phi$ , we generate a PDF with three variables that can be viewed as a cube of probability density. Figure 13 displays the more intense part of the cube as a white cloud and presents the projection of the function on three orthogonal planes.

#### Porosity sections comparison

In the 3D MF region, we generated 200 realizations, simulating porosity in a 493,092 point grid. The horizontal spacing is divided by two compared with previous results, meaning that for a given time, a seismic bin is now represented by four points. Half of the realizations used only  $I_P$  as a secondary attribute, whereas the other half incorporated  $I'_S$  to further constrain the process. Figure 14 shows the comparison between one realization of each approach.

Both methods provide better resolution of the intra-MF structure compared with previous results that modeled the complete forma-

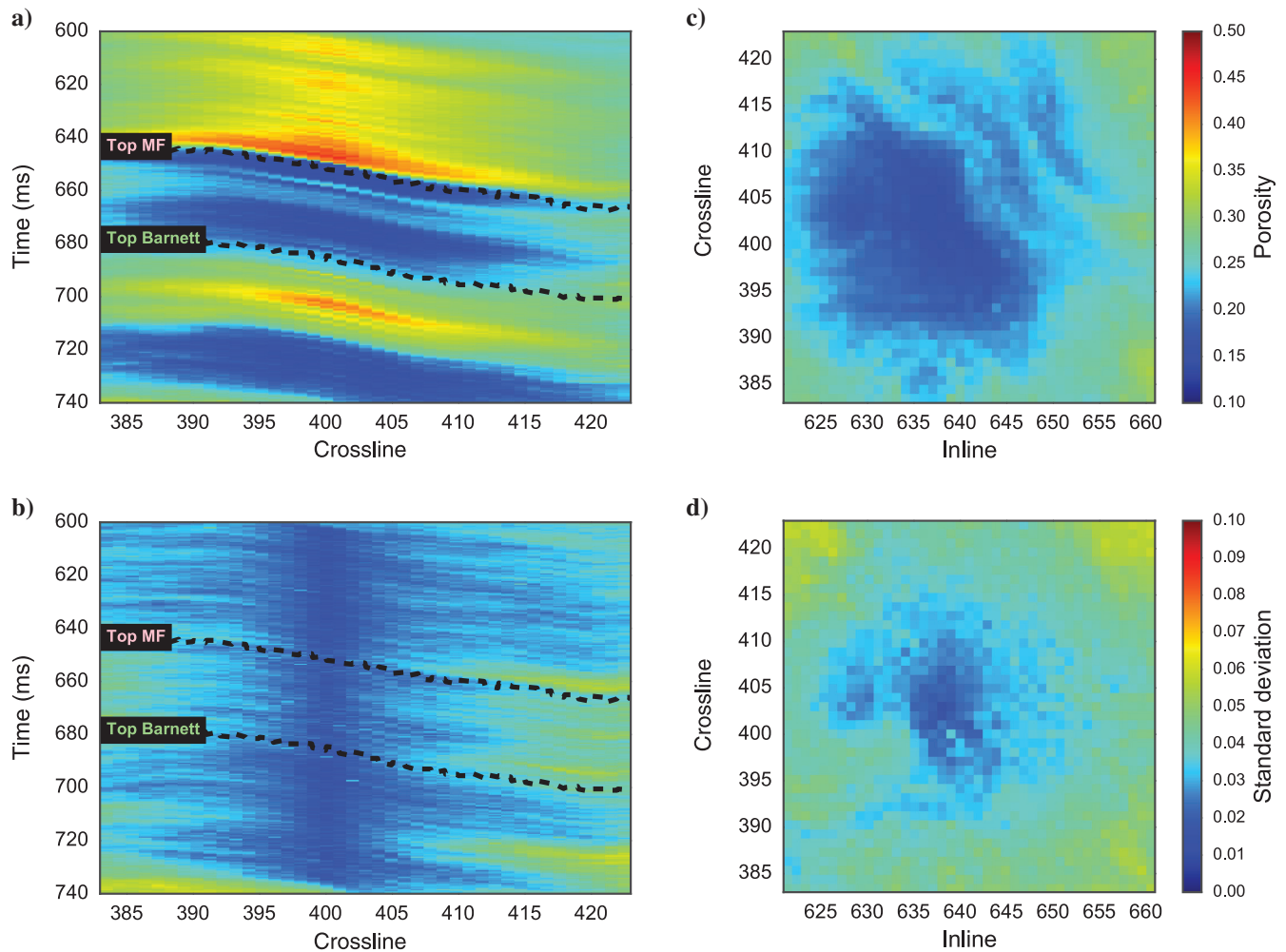


Figure 10. Mean and standard deviation pixel by pixel of the 100 high-resolution simulations. (a) Mean vertical panel at inline = 641 with (b) its associated standard deviation, (c) mean horizontal slice at time = 670 ms with (d) its associated standard deviation.

tion as a whole. Indeed, using statistics adapted to the formation (two low-porosity families) in the prior helps to delineate such features, especially at this resolution. Both results (with or without the second constraint), reproduce features that exhibit similar shapes. On the other side, from this realization, this algorithm generates more extreme values in the top part of Figure 14. This observation can be confirmed by looking at the mean and standard deviation of one panel for each scenario (Figure 15).

From Figure 15b, we see that our realizations are quite well-constrained with a weak standard deviation when using only  $I_P$  as a secondary attribute. As  $I'_S$  is added to constrain the simulation (Figure 15d), the standard deviation decreases even more, especially in low-porosity areas. Putting Figure 15a against Figure 15c, we also rise to the conclusion that when using only  $I_P$ , high-porosity areas show higher maximum.

## DISCUSSION

The proposed methodology succeeded in stochastically simulating porosity in a 3D volume and at a desired resolution. It used a stochastic downscaling procedure that helps to take into account the

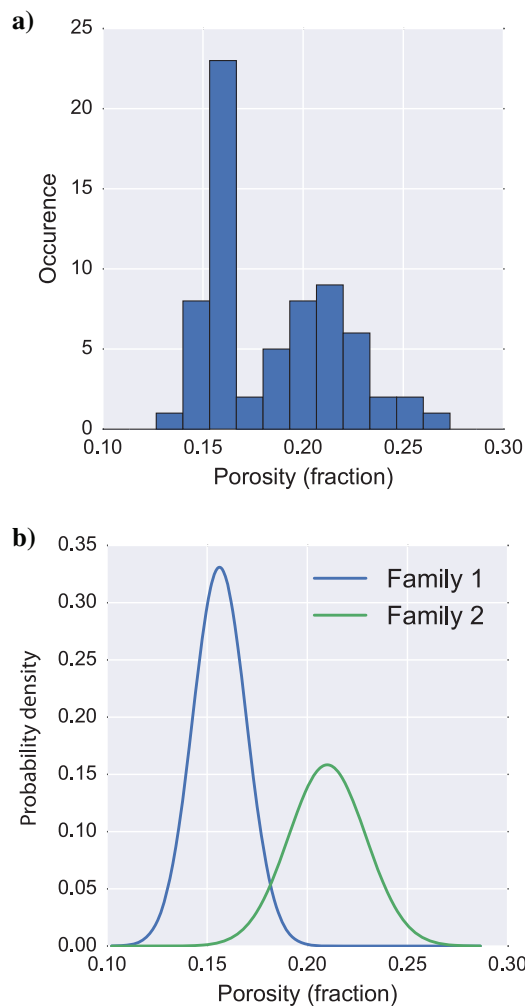


Figure 11. (a) Histogram of porosity data at well 1 upscaled at resolution of 0.5 ms limited to the MF formation and (b) modeled PDF of each family of the MF from bimodal GMM approximation.

difference of scale between the hard data measured at the well log and the impedance inverted from seismic data. It was shown that realizations at the seismic scale might not have a desirable level of intraformation feature definition, but they achieve the reproduction of large-scale variations and introduce some level of heterogeneity within. When integrating downscaling in the workflow, undesirable averaging may occur when geologic facies in presence have a significant difference in their primary variable statistics (mean and variance). For example, on the histogram in Figure 9d, we observe a skew toward high porosity. Moreover, Figures 7b and 10b show different variations in the lateral direction. In Figure 7b, the nonporous formation (blue color, second and fourth layers in Figure 7a) has a longer lateral connection (the lower uncertainty marked in dark blue). However, in Figure 10b, porous formations (the yellow and red colors, the first and third layers in Figure 10a) have lower uncertainty than the second and fourth formations. This is a direct effect of the resolution change using the proposed methodology, and it can be explained by the shape of the bivariate downscaling PDF (Figure 8) and by equation 7. Thus, in some cases and at some scales, it has been shown to be more suitable to work formation by formation as we did to estimate porosity for the MF in the last part of the “Results” section.

The workflow presented is designed to achieve stochastic realizations of a variable of interest correlated to low-resolution and highly sampled secondary data. In the particular case of reservoir characterization for the hydrocarbon industry, it is made to extract information from the results of a deterministic stratigraphic inversion (poststack or prestack) and comes with its limitations. Deterministic inversion results are smooth estimates of the inverted parameters and provide a unique solution to a problem that can have many. Using a unique, best-estimate solution results in poor estimation of the tails of the distribution of the inverted parameter (Francis, 2006). Sauvageau et al. (2014) show that the usage of stochastic seismic inversion as an input for the BSS helps to reproduce the tails of the distribution of the variable of interest.

The proposed approach implies that the impedance inversion is equally accurate throughout the cube. However, the seismic inversion accuracy depends on the quality of the input seismic traces, which we can expect not to be constant throughout our study area. To improve our methodology, an accuracy quantity defined cell by

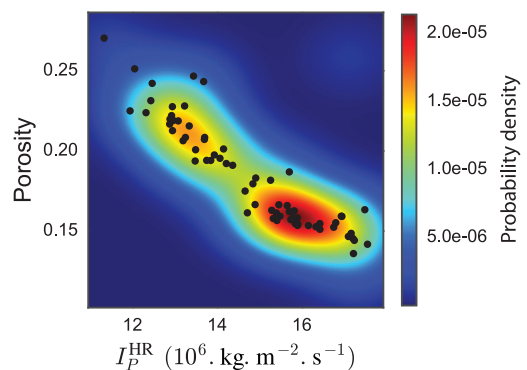


Figure 12. Bivariate PDF for the MF generated by 67 collocated well-log measurements (black dots) of the acoustic impedance ( $10^6 \text{ kg m}^{-2} \text{ s}^{-1}$ ) and porosity. The red color represents a high density of probability, whereas blue refers to a low density of probability.

cell could be added to increase global uncertainty and take this phenomenon into account.

The BSS algorithm used in this study does not force any constraint on the posterior distribution of porosity. As shown, the re-

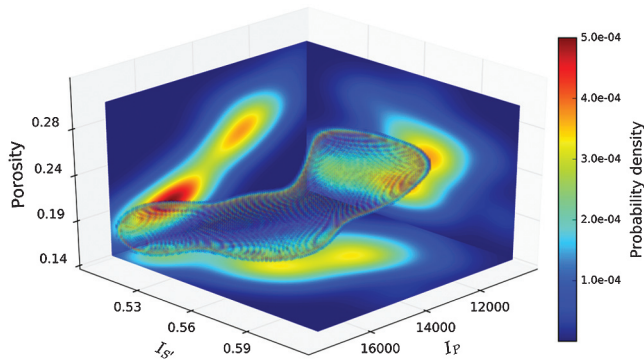


Figure 13. The 3D PDF generated by 67 collocated upscaled well-log measurements of three variables. The white cloud shows the more intense part of the kernel. Projections of the function are presented on three orthogonal planes, which show the bivariate relationship among the three pair of variables. The  $I_S'$  being viewed as a ratio (adimensional) and  $I_P$  in  $10^6 \text{ kg m}^{-2} \text{ s}^{-1}$ .

sulting histogram represents a compromise between the likelihood function and the prior inferred from hard data. In the case study we presented, this does not present itself as an issue. Indeed, imposing the histogram of a single well over a large domain does not come as an obvious and constraint.

Following the methodology presented in this paper, it could be argued that the assumption made is that all variations in  $I_P$  and in another case  $I_P$  and  $I_S'$  are related to changes in porosity. However, the bandwidth chosen in our joint relationships (2D and 3D case) can account for uncoupled variations between the primary and secondary variables. Nevertheless, it remains that the process of determining this parameter is user dependent and difficult to QC. Although being data driven (it is determined from dispersion of the scatter plot), the bandwidth of the kernel is a more or less free parameter and exhibits a strong influence on the resulting estimate. A solution to that issue could be to base the bandwidth parameter on an actual petrophysical relationship.

## CONCLUSION

In this paper, we presented a workflow that uses the BSS algorithm and applied it to a subarea of the Fort Worth Basin and then only to the MF. Three different methodologies have been applied to stochas-

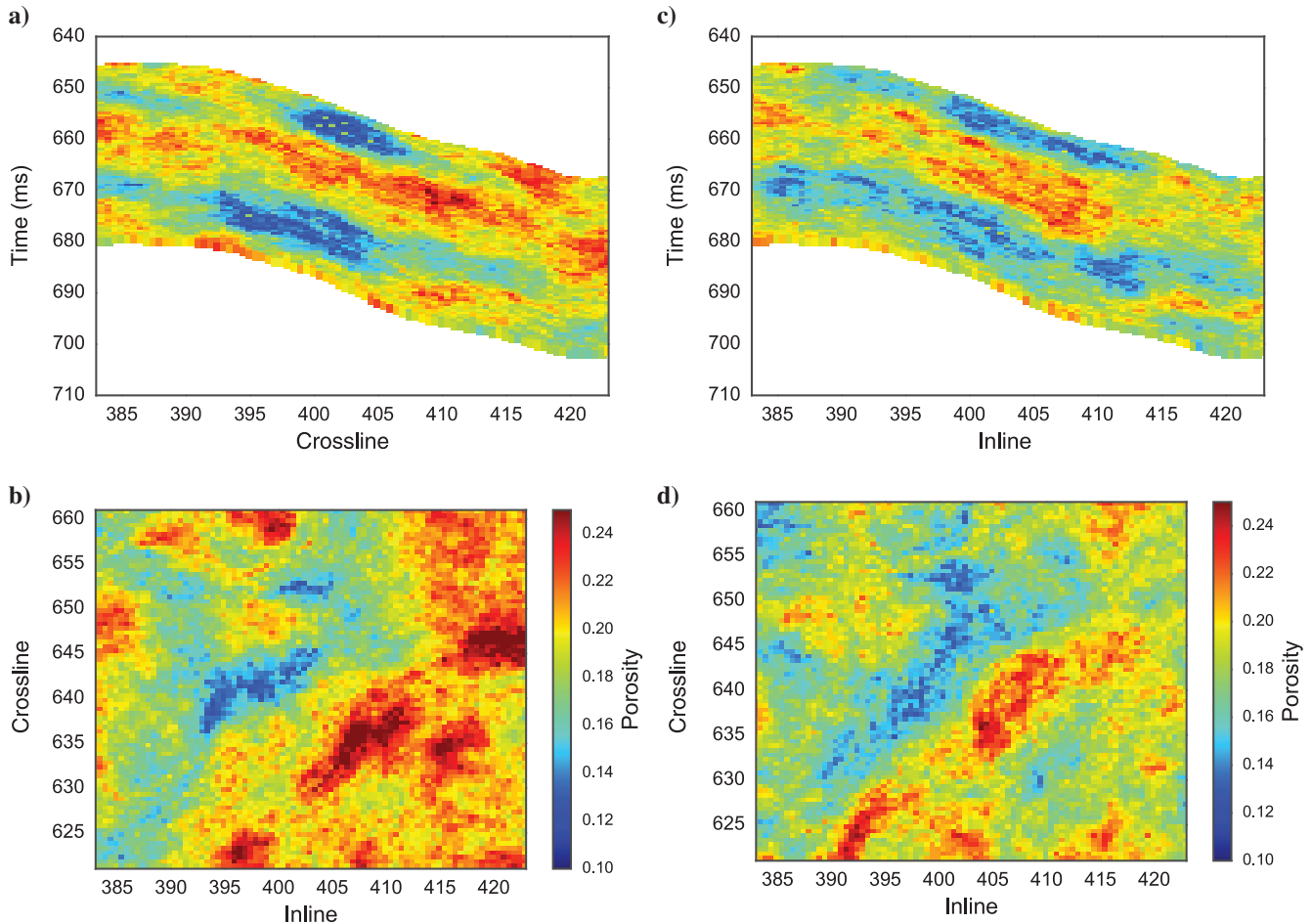


Figure 14. Porosity realization example using only  $I_P$  as secondary attribute (top) and using  $I_P$  and  $I_S'$  in the relationship (bottom). (a-c) Panel for inline = 640 and (b-d) time slice at  $t = 674 \text{ ms}$ .

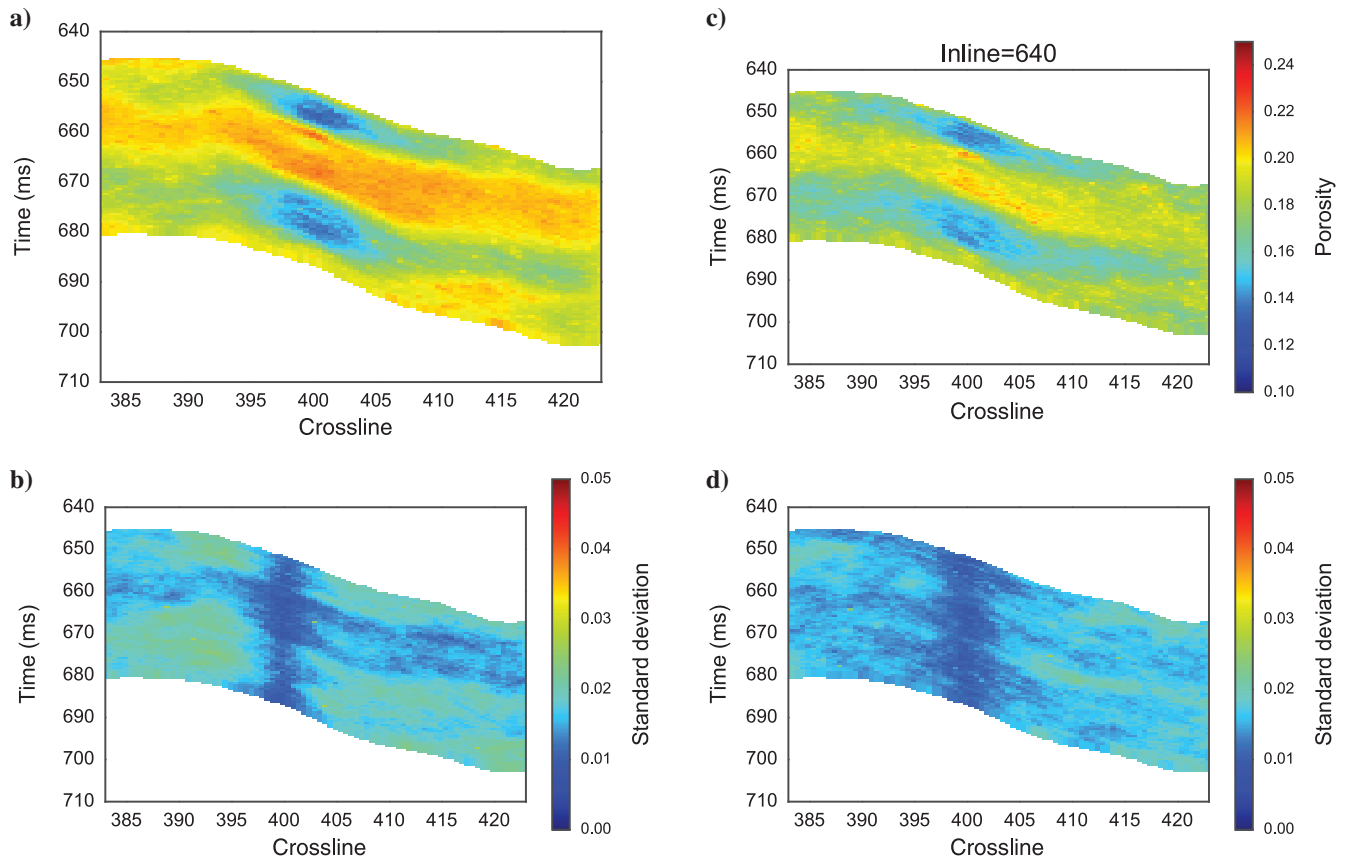


Figure 15. Mean and standard deviation of 100 porosity realizations for each scenario, using only  $I_p$  as secondary attribute (top) and using  $I_p$  and  $I'_s$  in the relationship (bottom). (a-c) Mean panel for inline = 640, and (b-d) standard deviation panel for inline = 640.

tically simulate porosity at the seismic scale or at a higher resolution, using one or two constraints as secondary data in the likelihood function. For each case, 100 realizations were computed, honoring available hard data and respecting the expected geologic set up.

Although the workflow accounts for some uncertainty, it does not account for the significant error inherent to the seismic inversion process. Including it in the calculation of our posterior distribution would definitely bring the standard deviation to much higher values, especially in the case with two constraints from the inversion process.



Nevertheless, the algorithm proved to be flexible because it gives the possibility to work with nonlinear and non-Gaussian statistical relationships between collocated well data or for downscaling purposes. It also proven to be straightforward to implement and not too computationally intensive. Indeed, the part that is computationally intensive is the kriging step, and this can be alleviated using a neighborhood. Finally, we found it to be comprehensive because it is easy **3** to explain to team members less familiar with geostatistics.

## REFERENCES

- Adelinet, M., A. Barnoud, V. Clochard, and P. Ricarte, 2013, Improved unconventional reservoir characterization using multi-azimuth stratigraphic inversion, case study on the Fort Worth Basin: *Journal of Unconventional Oil and Gas Resources*, **3**, 15–26, doi: [10.1016/j.juogr.2013.10.001](https://doi.org/10.1016/j.juogr.2013.10.001).
- Adelinet, M., J. Fortin, and Y. Gueguen, 2011, Dispersion of elastic moduli in a porous-cracked rock: Theoretical predictions for squirt-flow: *Tectonophysics*, **503**, 173–181, doi: [10.1016/j.tecto.2010.10.012](https://doi.org/10.1016/j.tecto.2010.10.012).
- Adelinet, M., and M. Le Ravalec, 2015, Effective medium modeling: How to efficiently infer porosity from seismic data?: *Interpretation*, **3**, no. 4, SAC1–SAC7, doi: [10.1190/INT-2015-0065.1](https://doi.org/10.1190/INT-2015-0065.1).
- Batzle, M., and Z. Wang, 1992, Seismic properties of pore fluids: *Geophysics*, **57**, 1396–1408, doi: [10.1190/1.1443207](https://doi.org/10.1190/1.1443207).
- Batzle, M. L., D. H. Han, and R. Hofmann, 2006, Fluid mobility and frequency-dependent seismic velocity-direct measurements: *Geophysics*, **71**, no. 1, N1–N9, doi: [10.1190/1.2159053](https://doi.org/10.1190/1.2159053).
- Bosch, M., T. Mukerji, and E. F. Gonzalez, 2010, Seismic inversion for reservoir properties combining statistical rock physics and geostatistics: A review: *Geophysics*, **75**, no. 5, 75A165–75A176, doi: [10.1190/1.3478209](https://doi.org/10.1190/1.3478209).
- Bowker, K. A., 2007, Development of the Barnett Shale Play, Fort Worth Basin: *AAPG Bulletin*, **91**523–533, doi: [10.1306/06190606018](https://doi.org/10.1306/06190606018).
- Doyen, P. M., 1988, Porosity from seismic data: A geostatistical approach: *Geophysics*, **53**, 1263–1275, doi: [10.1190/1.1442404](https://doi.org/10.1190/1.1442404).
- Doyen, P. M., T. Guidish, and M. de Buyl, 1989, Seismic discrimination of lithology in sand/shale reservoirs: A Bayesian approach: 59th Annual International Meeting, SEG, Expanded Abstracts, 719–722.
- Doyen, P. M., D. E. Psaila, L. D. den Boer, and D. Jans, 1997, Reconciling data at seismic and well log scales in 3-D earth modelling: Presented at the SPE Annual Technical Conference and Exhibition.
- Dubreuil-Boisclair, C., E. Gloaguen, G. Bellefleur, and D. Marcotte, 2012, Non-Gaussian gas hydrate grade simulation at the Mallik site, Mackenzie Delta, Canada: *Marine and Petroleum Geology*, **35**, 20–27, doi: [10.1016/j.marpetgeo.2012.02.020](https://doi.org/10.1016/j.marpetgeo.2012.02.020).
- Dubreuil-Boisclair, C., E. Gloaguen, D. Marcotte, and B. Giroux, 2011, Heterogeneous aquifer characterization from ground-penetrating radar tomography and borehole hydrogeophysical data using nonlinear Bayesian simulations: *Geophysics*, **76**, no. 4, J13–J25, doi: [10.1190/1.3571273](https://doi.org/10.1190/1.3571273).
- Dubrule, O., 2003, Geostatistics for seismic data integration in earth models (DISC No. 6): SEG, 1–25.
- Erlich, R. N., and J. L. Coleman Jr., 2005, Drowning of the Upper Marble Falls carbonate platform (Pennsylvanian), central Texas: A case of conflicting signals?: *Sedimentary Geology*, **175**, 479–499, doi: [10.1016/j.sedgeo.2004.12.017](https://doi.org/10.1016/j.sedgeo.2004.12.017).

- Fang, Z., and D. Yang, 2015, Inversion of reservoir porosity, saturation, and permeability based on a robust hybrid genetic algorithm: *Geophysics*, **80**, no. 5, R265–R280, doi: [10.1190/geo2014-0502.1](https://doi.org/10.1190/geo2014-0502.1).
- Francis, A. M., 2006, Understanding stochastic inversion: *First Break*, **24**, 69–77, doi: [10.3997/1365-2397.2006026](https://doi.org/10.3997/1365-2397.2006026).
- Gassmann, F., 1951, Elastic waves through a packing of spheres: *Geophysics*, **16**, 673–685, doi: [10.1190/1.1437718](https://doi.org/10.1190/1.1437718).
- Goovaerts, P., 2000, Geostatistical approaches for incorporating elevation into the spatial interpolation of rainfall: *Journal of Hydrology*, **228**, 113–129, doi: [10.1016/S0022-1694\(00\)00144-X](https://doi.org/10.1016/S0022-1694(00)00144-X).
- Grana, D., 2014, Probabilistic approach to rock physics modeling: *Geophysics*, **79**, no. 2, D123–D143, doi: [10.1190/geo2013-0333.1](https://doi.org/10.1190/geo2013-0333.1).
- Grana, D., and E. Della Rossa, 2010, Probabilistic petrophysical-properties estimation integrating statistical rock physics with seismic inversion: *Geophysics*, **75**, no. 3, O21–O37, doi: [10.1190/1.3386676](https://doi.org/10.1190/1.3386676).
- Haas, A., and O. Dubrule, 1994, Geostatistical inversion: A sequential method of stochastic reservoir modeling constrained by seismic data: *First Break*, **12**, 561–569, doi: [10.3997/1365-2397.1994034](https://doi.org/10.3997/1365-2397.1994034).
- Hammersley, J., 2013, Monte Carlo methods: Springer Science and Business Media.
- Le Ravalec, M., B. Doligez, and O. Lerat, 2014, Integrated reservoir characterization and modeling: Ebook: IFP Energies Nouvelles.
- Marroquin, I. D., 2015, Automated seismic facies for data integration: An example from Fort Worth Basin, Texas (USA): *First Break*, **33**, 51–62, doi: [10.3997/1365-2397.2015001](https://doi.org/10.3997/1365-2397.2015001).
- Matheron, G., H. Beucher, and C. de Fouquet, 1987, Conditional simulation of the geometry of Fluvio-deltaic reservoirs: Presented at the SPE Annual Technical Conference and Exhibition.
- Montgomery, S. L., D. M. Jarvie, K. A. Bowker, and R. M. Pollastro, 2005, Mississippian Barnett Shale, Fort Worth basin, north-central Texas: Gas-shale play with multi-trillion cubic foot potential: *AAPG Bulletin*, **89**, 155–175, doi: [10.1306/09170404042](https://doi.org/10.1306/09170404042).
- Naeem, M., H. M. El-Araby, M. K. Khalil, M. K. Jafri, and F. Khan, 2015, Integrated study of seismic and well data for porosity estimation using multi-attribute transforms: A case study of Boonsville Field, Fort Worth Basin, Texas, USA: *Arabian Journal of Geosciences*, **8**, 8777–8793, doi: [10.1007/s12517-015-1806-7](https://doi.org/10.1007/s12517-015-1806-7).
- Parzen, E., 1962, On estimation of a probability density function and mode: *The Annals of Mathematical Statistics*, **33**, 1065–1076, doi: [10.1214/aoms/1177704472](https://doi.org/10.1214/aoms/1177704472).
- Pollastro, R. M., D. M. Jarvie, R. J. Hill, and C. W. Adams, 2007, Geologic framework of the Mississippian Barnett Shale, Barnett-Paleozoic total petroleum system, Bend Arch, Fort Worth Basin: *Texas AAPG Bulletin*, **91**, 405–436, doi: [10.1306/10300606008](https://doi.org/10.1306/10300606008).
- Pyrcz, M. J., and C. V. Deutsch, 2014, *Geostatistical reservoir modeling*: Oxford University Press.
- Rosenblatt, M., 1956, Remarks on some nonparametric estimates of a density function: *The Annals of Mathematical Statistics*, **27**, 832–837, doi: [10.1214/aoms/1177728190](https://doi.org/10.1214/aoms/1177728190).
- Ruggeri, P., J. Irving, E. Gloaguen, and K. Holliger, 2013, Regional-scale integration of multiresolution hydrological and geophysical data using a two-step Bayesian sequential simulation approach: *Geophysical Journal International*, **194**, 289–303, doi: [10.1093/gji/ggt067](https://doi.org/10.1093/gji/ggt067).
- Sauvageau, M., E. Gloaguen, M. Claprood, R. Lefebvre, and M. Beche, 2014, Multimodal reservoir porosity simulation: An application to a tight oil reservoir: *Journal of Applied Geophysics*, **107**, 71–79, doi: [10.1016/j.jappgeo.2014.05.007](https://doi.org/10.1016/j.jappgeo.2014.05.007).
- Silverman, B., 1986, *Density estimation for statistics and data analysis*: Chapman and Hall.
- Tarantola, A., 1984, Inversion of seismic reflection data in the acoustic approximation: *Geophysics*, **49**, 1259–1266, doi: [10.1190/1.1441754](https://doi.org/10.1190/1.1441754).
- Wand, M. P., and M. C. Jones, 1995, *Kernel smoothing*: Monographs on statistics and applied probability: Chapman and Hall.

# Queries

1. Please provide an abbreviated (i.e., less than 38 characters) title for the running header 
2. Please replace “in a subsequent section” with the section name. 
3. An acknowledgments section is not provided in this article. Please check and confirm.

